GLL
Geomatics, Landmanagement and Landscape No. 2 • 2026, 35–57

ISSN 2300-1496 https://doi.org/10.15576/GLL/224290

Research paper

Received: 31.01.2026
Accepted: 08.06.2026
Published: 30.06.2026

Land cover change and surface thermal patterns in the Upper Silesian–Dąbrowa Basin Metropolis, 1986–2023

Ewa Głowienka[1,] ✉ 0000-0001-7326-1592
Tymoteusz Maj[1] 0009-0002-2430-7982

[1] Department of Photogrammetry, Remote Sensing of Environment and Spatial Engineering, AGH University of Krakow
✉ Corresponding author: eglo@agh.edu.pl

Summary

Urban expansion in polycentric postindustrial regions alters land cover and surface thermal patterns. This study assessed how these processes evolved in the Upper Silesian–Dąbrowa Basin Metropolis (Górnośląsko-Zagłębiowska Metropolia, hereafter GZM), Poland, between 1986 and 2023, using multi-temporal Landsat data. UAV thermal imagery was used only to support the local interpretation of selected thermal contrasts. The LULC classification distinguished four broad classes: agricultural land, anthropogenic surfaces, forest areas, and water bodies. Over the study period, anthropogenic surfaces increased overall, whereas agricultural land declined. Forest areas remained an important part of the metropolitan landscape, although their spatial pattern became more fragmented and its total share decreased by the end of the study period. The transition matrix showed that the main land cover conversion was from agricultural land to anthropogenic surfaces, indicating that urban growth occurred mainly at the expense of open/non-forest vegetated land. LST patterns were closely related to land cover. The highest temperatures occurred in built up, industrial, and transport areas, whereas lower values were associated with forest and water surfaces. Areas of elevated summer LST became more continuous within the metropolitan core, especially along major transport corridors. UAV imagery revealed pronounced local thermal contrasts within warm Landsat pixels, but it was treated as qualitative support rather than direct validation of satellite derived temperatures. Overall, the results show that long term land cover change played a major role in shaping the thermal structure of the GZM and provide spatially explicit information relevant to planning and climate adaptation.

Keywords

Landsat • land surface temperature • land cover transitions • postindustrial metropolis • UAV • thermal survey • blue-green infrastructure

1. Introduction

Urban growth alters the physical character of the land surface. As sealed surfaces expand and biologically active land declines, runoff, moisture availability, and heat storage change as well. Surface temperature is not the same as air temperature, but it remains a useful indicator of how land cover, surface materials, and moisture conditions shape the thermal pattern of cities. For that reason, land cover change and land surface temperature are often examined together in remote sensing studies of metropolitan areas [Voogt and Oke 2003, Weng 2009].

Many Landsat based studies have shown that warmer surfaces tend to be associated with built-up and impervious land cover, while vegetation generally weakens surface heating. This correlation is usually expressed as a negative link between LST and vegetation abundance and a positive association between LST and urban development intensity, although its strength varies with scale, season, and urban form [Weng et al. 2004, Xian and Crane 2006, Zhao et al. 2025, Rees et al. 2024].

Long Landsat archives are especially useful in this context because they allow consistent comparison over several decades using the same family of sensors. When combined with spectral indices and GIS based change analysis, they make it possible to track both structural land cover transformation and the evolution of thermal patterns over time. This remains one of the clearest strengths of satellite remote sensing in urban environmental studies [Roy et al. 2014, Głowienka et al. 2017, Manapragada et al. 2025].

The Upper Silesian–Dąbrowa Basin Metropolis is well suited to this kind of analysis. It is a large polycentric urban region with dense settlement, industrial and postindustrial land, a complex transport network, and fragmented green space. Recent studies from southern Poland have already shown that this spatial structure produces pronounced summer thermal contrasts and a distinct surface urban heat island pattern [Zuzańska-Żyśko and Sitek 2018, Renc et al. 2022, Renc and Łupikasza 2024].

The contribution of this study does not lie merely in extending the observation period by one year. Instead, it lies in combining long-term land cover change, class transitions, and thermal patterns within one metropolitan-scale analysis. Recent work by the authors in Krakow has likewise shown that built-up intensity, vegetation loss, and the spatial arrangement of urban green areas are closely related to surface thermal conditions. High resolution thermal observations can also help explain the internal structure of warm satellite pixels, even when they cannot be used as direct seasonal validation of absolute LST values [Głowienka and Micek 2025, Głowienka and Kucza 2025, Heinemann et al. 2020, Coutts et al. 2016, Głowienka et al. 2025].

The study therefore examined whether long term urban growth in the GZM was accompanied by an increase in anthropogenic surfaces and a decline in agricultural land, whether these changes were reflected in the spatial pattern of LST, and whether conversion from agricultural land to anthropogenic surfaces formed the main pathway of change. It also considered whether UAV thermal imagery could help interpret local thermal contrasts within warm Landsat pixels that remain unresolved at 30 m resolution.

2. Study area and methodology

2.1. Study area

The Upper Silesian–Dąbrowa Basin Metropolis (GZM), located in southern Poland, occupies more than 2,500 km² and includes 41 municipalities. Its spatial structure is polycentric and combines dense residential areas, industrial and postindustrial land, extensive transport infrastructure, and fragmented green space. This land cover heterogeneity makes the GZM a suitable case for analysing links between long-term land cover change and surface thermal patterns [Zuzańska-Żyśko and Sitek 2018].

The region lies within the Silesian Highlands, where relief and valley systems influence local air circulation at the local scale. At the same time, dense built-up areas, widespread sealed surfaces, industrial zones, and discontinuous green corridors favour strong thermal contrasts. For this reason, thermal patterns in the GZM are shaped not only by individual city centres, but also by the arrangement of industrial land, transport corridors, peri-urban development, and larger forest complexes.

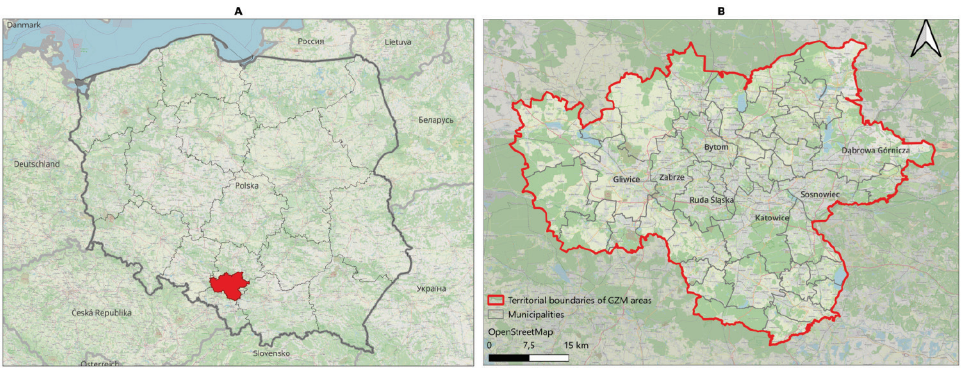

Source: Authors' own study

Fig. 1. Location of the Upper Silesian–Dąbrowa Basin Metropolis within Poland (left) and its municipal structure within the study area (right). The red outline marks the external boundary of the GZM, while thin grey lines show municipal boundaries. Major cities mentioned in the text are labelled.

2.2. Data

The satellite analysis was based on eight reference years: 1986, 1990, 1996, 2001, 2006, 2010, 2016, and 2023. Separate Landsat scenes were used for LULC classification and LST analysis when the most suitable acquisitions for land cover discrimination and thermal analysis did not coincide on the same date. For LULC mapping, preference was given to cloud free scenes from late summer and early autumn. For LST analysis, summer scenes were selected to reduce seasonal bias in surface temperature.

The reference years were not chosen to create equal temporal intervals, but to select the best available scenes for long term comparison. Each selected year provided a cloud

Table 1. Overview of datasets and their technical specifications used for LULC classification and LST analysis in the Upper Silesian–Dąbrowa Basin Metropolis

Dataset / Source	Type / Format	Acquisition date	Platform	Cloud cover / Conditions	Purpose / Use in analysis	Provider
UAV thermal survey	RGB + thermal (640×512 px)	05 January 2024	DJI M300 RTK + Zenmuse XT2	Clear sky; low wind (< 2 m/s)	High resolution thermal imagery used for local interpretation of thermal contrasts and qualitative cross scale comparison with Landsat thermal patterns	NaviGate
Administrative boundaries (GZM)	SHP / GML	2023	–	–	Masking study area	GIS Support

poor acquisition with full coverage of the GZM and seasonal conditions suitable for either LULC mapping or LST analysis. The series begins in 1986 because it is the earliest year in the adopted TM/OLI/TIRS framework for which a scene meeting these criteria was available. Earlier dates, such as 1980, would require Landsat MSS data with different spatial and spectral characteristics, which would reduce comparability with the later 30 m TM/OLI record. Intermediate years such as 1996 and 2001 were retained because they captured relevant stages of metropolitan restructuring and offered scenes of acceptable quality rather than because of a rigid fixed interval.

Landsat 5 TM, Landsat 8 OLI/TIRS, and Landsat 9 OLI-2/TIRS-2 data were accessed in Google Earth Engine. Reflective bands and derived indices were used for LULC classification, whereas thermal analysis was based on the USGS Collection 2 Level-2 surface temperature product. All scenes were clipped to the GZM boundary and masked for clouds and cloud shadows using QA information. The scenes listed in Table 2 represent the final acquisitions used in the analysis rather than multi-scene seasonal composites.

The UAV component consisted of a thermal survey acquired on 5 January 2024 with a DJI Matrice 300 RTK platform equipped with a DJI Zenmuse XT2 radiometric thermal sensor. These data were used as a local comparative dataset to interpret selected thermal contrasts visible in Landsat imagery, not as a direct seasonal validation of summer satellite derived LST.

Administrative boundaries of the GZM were used to mask the study area and ensure consistent spatial reporting across all analyses.

Table 2. Summary of Landsat scenes and mission metadata used for LULC classification and LST analysis in the Upper Silesian–Dąbrowa Basin Metropolis (1986–2023)

Sensor	Date	Landsat scene (ID)	Cloud cover [%]
Landsat 5 TM	1986-10-16	LT05_L1TP_188025_19861016_20200917_02_T1	0
Landsat 5 TM	1990-10-11	LT05_L1TP_188025_19901011_20200915_02_T1	0
Landsat 5 TM	1996-08-24	LT05_L1TP_188025_19960824_20200911_02_T1	0
Landsat 5 TM	2001-07-28	LT05_L1TP_189025_20010728_20200905_02_T1	3
Landsat 5 TM	2006-09-12	LT05_L1TP_189025_20060912_20200831_02_T1	1
Landsat 5 TM	2010-09-23	LT05_L1TP_189025_20100923_20200823_02_T1	0
Landsat 5 TM	1986-08-04	LT05_L2SP_189025_19860804_20200918_02_T1	2
Landsat 5 TM	1990-08-31	LT05_L2SP_189025_19900831_20200915_02_T1	0
Landsat 5 TM	1996-08-24	LT05_L2SP_188025_19960824_20200911_02_T1	0
Landsat 5 TM	2001-07-28	LT05_L2SP_189025_20010728_20200905_02_T1	3
Landsat 5 TM	2006-07-03	LT05_L2SP_188025_20060703_20200831_02_T1	2

Table 2. cont.

Sensor	Date	Landsat scene (ID)	Cloud cover [%]
Landsat 5 TM	2010-08-22	LT05_L2SP_189025_20100822_20200823_02_T1	1
Landsat 8 OLI/TIRS	2016-09-16	LC08_L2SP_188025_20160916_20200906_02_T1	1
Landsat 8 OLI/TIRS	2016-07-21	LC08_L2SP_189025_20160721_20200906_02_T1	5.18
Landsat 8 OLI/TIRS	2023-07-09	LC08_L2SP_189025_20230709_20230718_02_T1	5.94
Landsat 9 OLI-2/ TIRS-2	2023-09-28	LC09_L2SP_188025_20230928_20230928_02_T1	0.02

Note: LULC classification and LST analysis were based on separate reference scenes when the most suitable acquisitions differed by application. The scenes listed here are the final acquisitions used in the analysis and do not represent annual median composites.

2.3. Methodology

The overall processing chain is summarised in Figure 2.

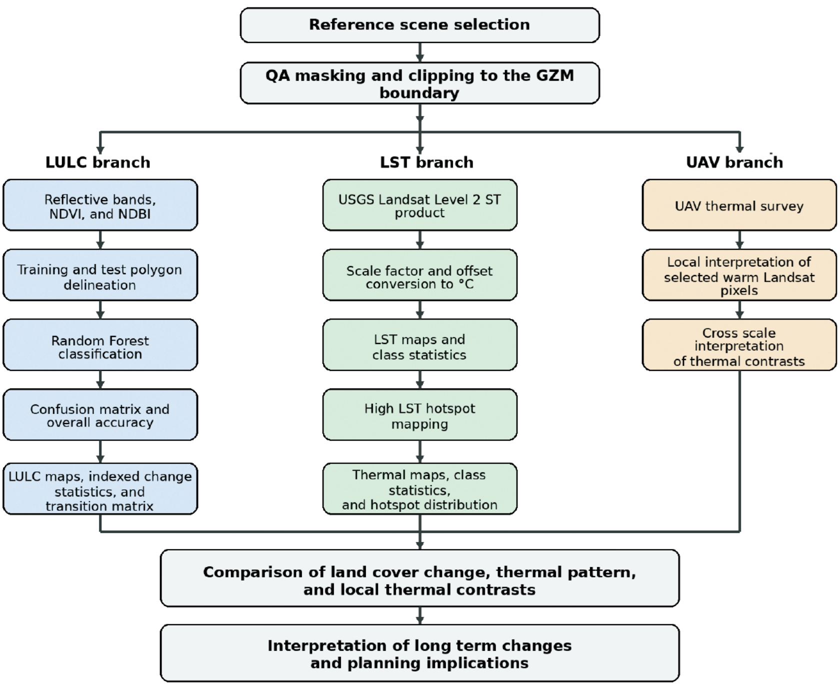

Source: Authors' own study

Fig. 2. Workflow used for scene selection, pre-processing, LULC classification, accuracy assessment, Landsat surface temperature analysis, and local interpretation of selected thermal contrasts using UAV imagery

All satellite processing steps were implemented in Google Earth Engine. Landsat images were imported from the USGS Collection 2 Level 2 archives, filtered by date, cloud cover, and study area intersection, and clipped to the GZM boundary. QA bands were used to mask clouds and cloud shadows. NDVI and NDBI were calculated from the surface reflectance bands. Training and test polygons were converted to pixel samples (30 m). The 'Random Forest' classifier was then applied separately to each reference year using the same group of predictor layers. The 'Random Forest' classifier was run with 10 trees. For thermal analysis, the Level 2 ST band was rescaled with the standard USGS factor and offset and then converted to degrees Celsius.

Input variables for LULC classification included reflective Landsat bands together with NDVI and NDBI. NDVI was used to describe vegetation activity, whereas NDBI was used to support the discrimination of built-up and other sealed surfaces. The indices were calculated as follows:

$$NDVI = \frac{NIR - RED}{NIR + RED} \tag{1}$$

[Rouse et al. 1973]

$$NDBI = \frac{SWIR - NIR}{SWIR + NIR} \tag{2}$$

[Zha et al. 2003]

LULC classification was performed with a supervised "Random Forest" classifier in Google Earth Engine using reflective Landsat bands together with NDVI and NDBI as auxiliary variables. Four broad classes were mapped: agricultural land, anthropogenic surfaces, forest areas, and water bodies. In this study, anthropogenic surfaces include built-up land, transport infrastructure, industrial sites, and other sealed or strongly transformed surfaces. This classification scheme was intentionally limited to broad categories because of the 30 m spatial resolution of Landsat imagery and the highly fragmented urban structure of the study area. Woodland was included within the forest class. Grass- and shrub-dominated surfaces were included in the agricultural land class, which therefore represents agricultural and other non-forest vegetated/open land. A more detailed legend was not adopted because the 30 m Landsat pixel and the highly fragmented structure of the GZM do not allow stable separation of these sub-classes across all eight reference years. High resolution imagery was therefore used only as ancillary material for visual interpretation, not as the primary classification source, because no spectrally consistent high resolution archive is available for the full 1986–2023 period.

Training data were prepared manually as homogeneous reference polygons representing the four classes in each analysed year. Their numbers by class and year are reported in Table 3. Polygon delineation was based on expert visual interpretation of Landsat imagery, including both natural colour and false colour composites, and was guided by the spatial continuity of land cover units and their spectral distinctiveness.

Spectral signatures were then extracted automatically from all Landsat pixels intersecting the training polygons using the 'sampleRegions' procedure at 30 m spatial resolution. Because the number of sampled pixels depended on polygon size and spatial configuration, the number of spectral signatures varied between years and classes, while the number of training polygons was controlled explicitly. The effectiveness of the classification was assessed using a confusion matrix (error matrix) derived from an independent set of test polygons, and overall accuracy was calculated as the proportion of correctly classified samples.

Classification accuracy was evaluated using an independent set of manually delineated test polygons that were not used during classifier training. Because the reference polygons were derived from image interpretation rather than field observations, accuracy assessment should be treated as image based internal validation rather than external ground validation. Across the analysed years, the number of training polygons ranged from 106 in 1986 to 238 in 2023, while the number of independent test polygons ranged from 59 to 126. Overall classification accuracy ranged from 90.23% to 94.26%, indicating satisfactory discrimination of the four broad land cover classes for multi-temporal comparison. Because the classification was intentionally limited to broad land cover classes, the transition results should be interpreted at the class level rather than as parcel scale land cover change.

Confusion matrices were computed separately for each reference year from the independent test polygons. Overall accuracy was calculated as the proportion of correctly classified validation samples in the full error matrix. Because the study is based on four broad classes designed for multi-temporal comparison, overall accuracy is used here as the main summary measure.

No field GPS campaign was carried out for this study, and no GPS reference points were used in either training or validation. The validation presented here is therefore based on independently delineated image interpretation polygons rather than field observations.

Land surface temperature (LST) was derived from the USGS Landsat Collection 2 Level 2 surface temperature product (ST_B6 for Landsat 5 and ST_B10 for Landsat 8/9), following the operational product framework described by Malakar et al. [2018]. Pixel values were converted using the standard scale factor and offset and then expressed in degrees Celsius. Because the Level-2 product already represents atmospherically corrected surface temperature, no additional emissivity correction was applied in the present analysis.

The resulting LST layers were used to produce maps for the eight reference years and change maps that indicate the spatial distribution of elevated summer surface temperature. In this study, pixels with LST > 30°C were treated as an operational hotspot class used for descriptive comparison between years. This threshold should not be interpreted as a direct measure of classical urban heat island intensity.

The UAV survey was used to support local interpretation of spatial thermal contrasts visible within the Landsat based thermal pattern. Because the UAV data were acquired in winter and at a different time of day than the satellite scenes, they were not used

Table 3. Number of manually delineated training and independent test polygons used for supervised LULC classification and accuracy assessment in the years selected for the analysis

Year	Land classification category										
	Agricultural land		Anthropogenic surfaces		Water bodies		Forest areas		All classes		Overall accuracy
	Training polygons	Test polygons	Training polygons	Test polygons	Training polygons	Test polygons	Training polygons	Test polygons	Training polygons	Test polygons	[%]
1986	18	12	37	15	33	14	18	18	106	59	91.63
1990	21	15	44	22	37	24	22	19	124	80	94.26
1996	25	19	47	24	35	23	21	19	128	85	93.47
2001	26	19	57	30	40	26	19	19	142	101	93.10
2006	29	26	50	30	39	26	26	19	144	101	93.19
2010	31	26	66	30	49	26	29	19	175	101	92.99
2016	27	22	68	38	50	27	32	19	177	106	90.23
2023	48	22	81	51	54	28	55	25	238	126	90.45

for direct validation of absolute Landsat derived summer LST. Instead, the comparison focused on whether relatively warm satellite pixels corresponded to impervious surfaces and fine scale local heat sources visible in the UAV imagery. No in situ radiometric surface temperature measurements were available for the Landsat acquisition dates, so local validation of absolute LST was not possible. The study therefore relied on the USGS Level 2 surface temperature product, whose methodology and validation have been described in Malakar et al. [2018] and Duan et al. [2021], and used UAV data only for local qualitative interpretation of thermal contrasts within selected warm pixels.

A same day satellite comparison was not possible because the available Landsat scene for 5 January 2024 was strongly affected by cloud cover over the local UAV study area. The UAV dataset therefore served as a complementary local reference for interpreting thermal structure under cloud free field conditions.

3. Results

Across the analysed years, the GZM shows a clear shift in the balance between anthropogenic and other land cover categories. The most visible pattern is the expansion of anthropogenic surfaces, especially in inter-city zones and suburban areas where residential development and infrastructure intensified over time (Fig. 3).

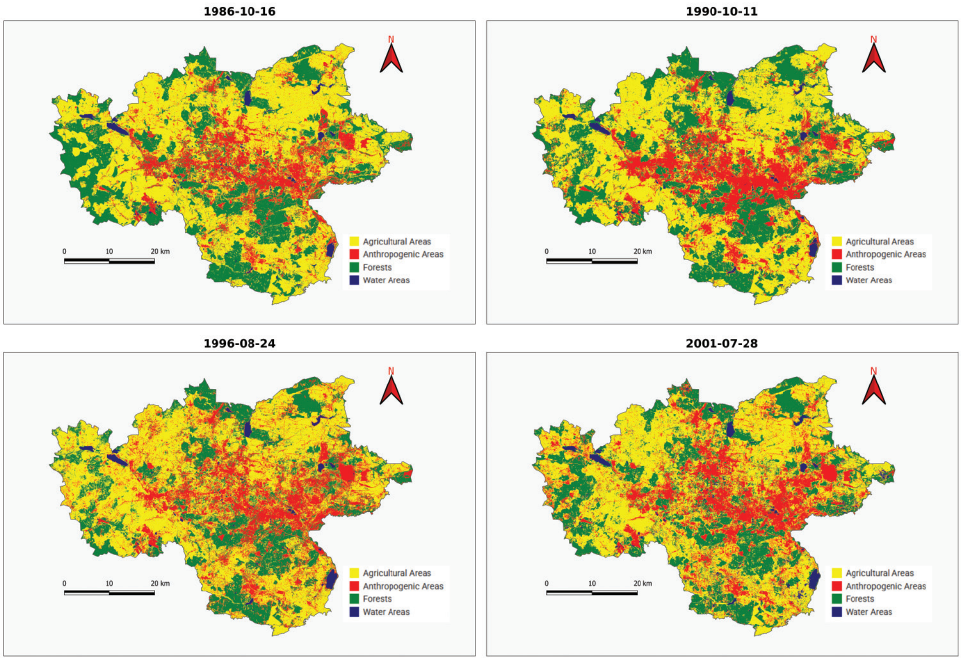

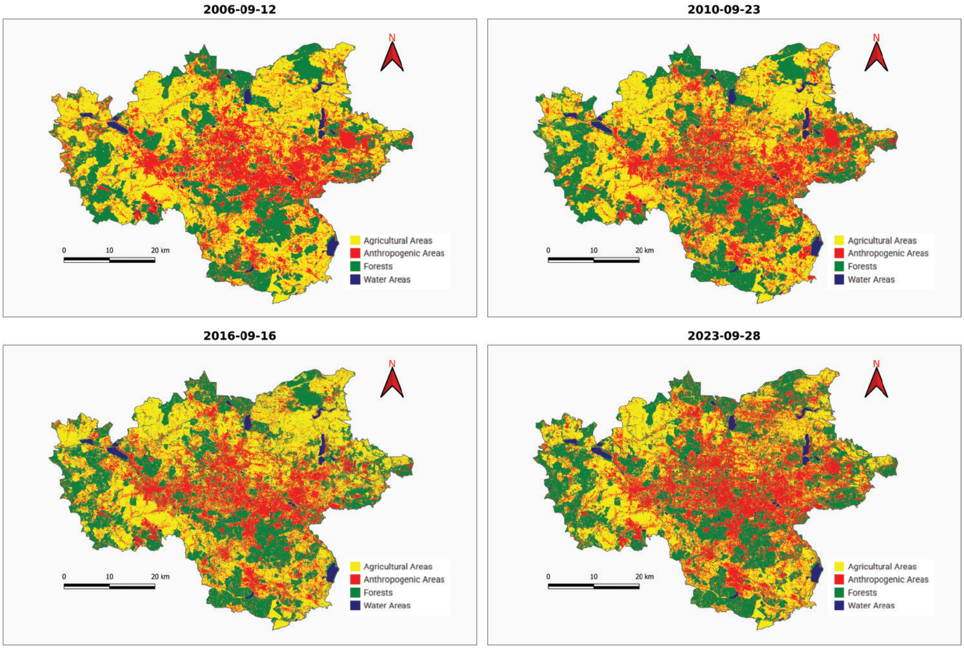

Source: Authors' own study

Fig. 3. Multi-temporal land use and land cover (LULC) classification maps derived from Landsat imagery for the Upper Silesian–Dąbrowa Basin Metropolis (1986–2023)

The LULC maps (Fig. 3) show a strong and persistent concentration of anthropogenic surfaces in the central part of the GZM, where this class consistently dominates the urban core. Over time, increasing fragmentation of land cover becomes evident, as previously homogeneous agricultural and forest areas are progressively subdivided into heterogeneous, mosaic-like spatial patterns typical of intensive suburbanisation.

The spatial arrangement of land cover classes exhibits a stable zonal structure (Fig. 3), with a central zone dominated by anthropogenic surfaces and peripheral areas characterised by a higher share of biologically active land, including forest areas and agricultural land. Water bodies remain relatively stable and are primarily represented as linear and point features. These patterns indicate that the most significant transformations concern the balance between built-up and vegetated surfaces.

A gradual decline in agricultural land is observed across the study period, while forest areas, although still spatially significant, exhibit increasing fragmentation and a slight overall decrease. These changes are primarily associated with urban expansion, infrastructure development, and land cover conversion in peri-urban areas. Additionally, part of the observed decline in forest cover may result from classification related effects, as fragmented or transitional vegetation patches may be spectrally assigned to other classes.

Table 4. Relative change in the extent of major LULC classes in the Upper Silesian–Dąbrowa Basin Metropolis, indexed to 1986 = 100. Values above 100 indicate expansion relative to 1986, whereas values below 100 indicate decline

Year	Agricultural land	Anthropogenic surfaces	Water bodies	Forest areas
1986	100.0	100.0	100.0	100.0
1990	92.5	142.3	101.9	71.8
1996	92.6	235.5	115.1	66.4
2001	92.3	251.5	125.3	65.7
2006	101.4	261.8	142.1	76.6
2010	101.1	330.2	119.4	81.4
2016	97.1	279.4	143.7	75.2
2023	90.6	305.4	131.1	62.6

When expressed as an index relative to 1986, anthropogenic surfaces show the strongest long term increase, while forest areas and agricultural land decline overall. Water bodies also increase moderately. This indexed format highlights the direction and magnitude of long-term class change while avoiding over-interpretation of uncertain absolute areal totals.

When viewed over the full study period, the dominant tendency is clear: anthropogenic surfaces expanded, whereas agricultural land declined. The intermediate fluctuations are visible, but they do not change the overall direction of change. Forest areas remained a major part of the metropolitan landscape, although its final pattern is more fragmented than at the beginning of the series.

A temporary weakening of the anthropogenic class signal appears between 2010 and 2016. This should not be interpreted as a real retreat of urban land. In a broad four class scheme applied to a fragmented postindustrial landscape, intermediate values are sensitive to redevelopment, vegetation encroachment on brownfields, and mixed pixels in transitional zones. For this reason, the long term direction of change is more informative than the fluctuation visible in a single interval.

Unlike Table 4, which presents relative class change indexed to 1986, Figure 4 shows the absolute area transferred between classes in km². The largest off diagonal transition is from agricultural land to anthropogenic surfaces (392.5 km²), which indicates that urban expansion occurred mainly at the expense of agricultural land. Other important transitions include agricultural land to forest areas (199.4 km²), forest areas to anthropogenic surfaces (106.0 km²), and anthropogenic surfaces to agricultural land (65.1 km²). Overall, these values show that land cover change in the GZM was not entirely one directional, but also involved vegetation succession and the reworking of postindustrial land.

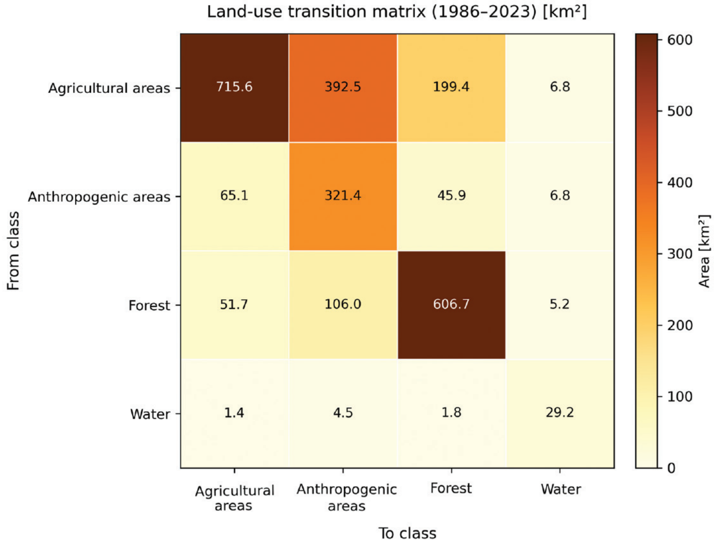

Source: Authors' own study

Fig. 4. Land cover transition matrix showing absolute areas of class to class conversions between 1986 and 2023 in the Upper Silesian–Dąbrowa Basin Metropolis, expressed in km^2. Unlike Table 4, which reports relative class change indexed to 1986, this matrix shows the area transferred between classes. Diagonal values indicate persistence, whereas off diagonal values represent conversion from one class to another

High diagonal values for agricultural land (715.6 km^2) and forest areas (606.7 km^2) indicate that substantial portions of the landscape remained stable despite ongoing transformations. Overall, the transition matrix confirms that the dominant structural process in the GZM is the progressive replacement of agricultural land by anthropogenic surfaces. The overall decline of the forest class should be interpreted cautiously. Part of it likely reflects real land conversion and fragmentation at urban and infrastructural edges, but part may also result from the difficulty of separating small woodland patches, shrub growth, and mixed vegetation within 30 m pixels. In the GZM, many forest complexes are dissected by roads, brownfields, and secondary succession surfaces, which increases class instability at boundaries.

Long-term proportional changes in LULC classes (Fig. 5) further support this interpretation, showing a net increase in anthropogenic surfaces and a decline in agricultural land.

Slight fluctuations and a moderate increase in water bodies are associated with the transformation of post-mining areas into artificial reservoirs, reflecting broader postindustrial landscape dynamics.

The thermal statistics show a stable ordering of LST across land cover classes. Anthropogenic surfaces were the warmest class in most years, whereas forest and water areas were generally cooler. Agricultural areas displayed intermediate and more variable thermal behaviour, which reflects differences in crop cover, soil exposure, and moisture conditions at the time of image acquisition.

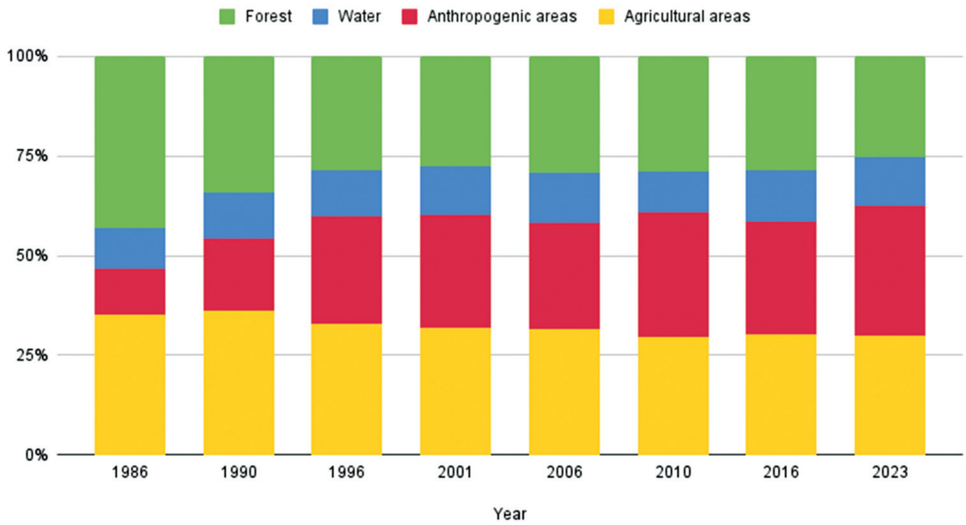

Source: Authors' own study

Fig. 5. Long-term changes in the percentage share of major land use and land cover (LULC) classes (agricultural, anthropogenic, water, and forest) in the Upper Silesian–Dąbrowa Basin Metropolis based on multi-temporal Landsat classifications (1986–2023)

These class level contrasts are consistent with the spatial pattern visible in Figure 6, where the warmest surfaces are concentrated in densely built-up, industrial, and transport zones, while larger forest complexes and moisture rich areas form cooler patches. The class ordering is also more stable than the absolute year-to-year values, which suggests that land cover structure is a more persistent control on the thermal pattern than short-term variation in any single scene.

Part of the increase in water bodies is likely related to the postindustrial transformation of former mining areas, including the emergence or expansion of artificial reservoirs [Renc et al. 2022].

The spatial distribution of LST closely corresponds to land cover structure, with elevated temperatures concentrated in areas dominated by impervious surfaces. The persistence of high temperature zones across multiple time points indicates a strong influence of stable land cover characteristics, including surface sealing, material properties, and reduced vegetation cover.

Temporal analysis shows an expansion and increasing spatial continuity of high temperature zones within the metropolitan core (Fig. 6). Thermal contrast between urban and vegetated areas also intensifies over time, reflecting the cumulative effects of urbanisation and infrastructure development.

Table 5. Mean land surface temperature (LST) [°C] across major LULC classes in the Upper Silesian–Dąbrowa Basin Metropolis (1986–2023)

Year	Land classification category				
	Agricultural land	Anthropogenic surfaces	Water bodies	Forest areas	Entire area
	mean temp [°C]	mean temp [°C]	mean temp [°C]	mean temp [°C]	mean temp [°C]
1986	30.07	36.15	23.16	27.73	30.39
1990	30.46	30.05	22.74	25.96	28.96
1996	24.83	27.21	19.70	22.28	24.63
2001	27.25	31.05	21.28	24.05	27.19
2006	32.20	36.35	25.89	27.50	31.92
2010	29.83	32.18	23.19	26.18	29.25
2016	29.72	32.93	24.46	26.11	29.31
2023	31.63	35.23	26.92	28.02	31.47

Note: Only mean LST is reported; minima and maxima are not shown because they are sensitive to residual anomalous pixels.

Areas of elevated summer LST, operationally defined here as pixels with LST > 30°C, were concentrated mainly in densely built-up and industrial zones and along major transport corridors (Fig. 7). Their extent and spatial continuity increased over time within the metropolitan core. Because the threshold is used here as a descriptive class rather than a formal UHI metric, the maps should be interpreted as an indicator of the distribution of elevated summer surface temperature.

In addition to compact clusters in city centres, elongated warm zones are visible along major infrastructure corridors. This pattern indicates that elevated LST is closely related to land cover structure, urban intensity, and the degree of surface sealing.

In the selected later scenes, elevated-LST zones spatially coincide with areas of intensified development and major transport corridors. In many places, zones with elevated temperatures can also be seen spreading along major roads, confirming their role as linear zones of elevated LST (Fig. 8). Areas with a stable or decreasing proportion of sealed surfaces show less dynamic thermal changes.

A more detailed comparison at the city scale (Fig. 8) confirms that the strongest thermal changes occur within the largest urban centres of the GZM. In Katowice, elevated temperatures are increasingly concentrated in central and southern districts. In Sosnowiec, thermal expansion is particularly evident in industrial and logistics areas, while in Gliwice, distinct thermal anomalies are associated with large industrial and warehouse complexes and major transport infrastructure.

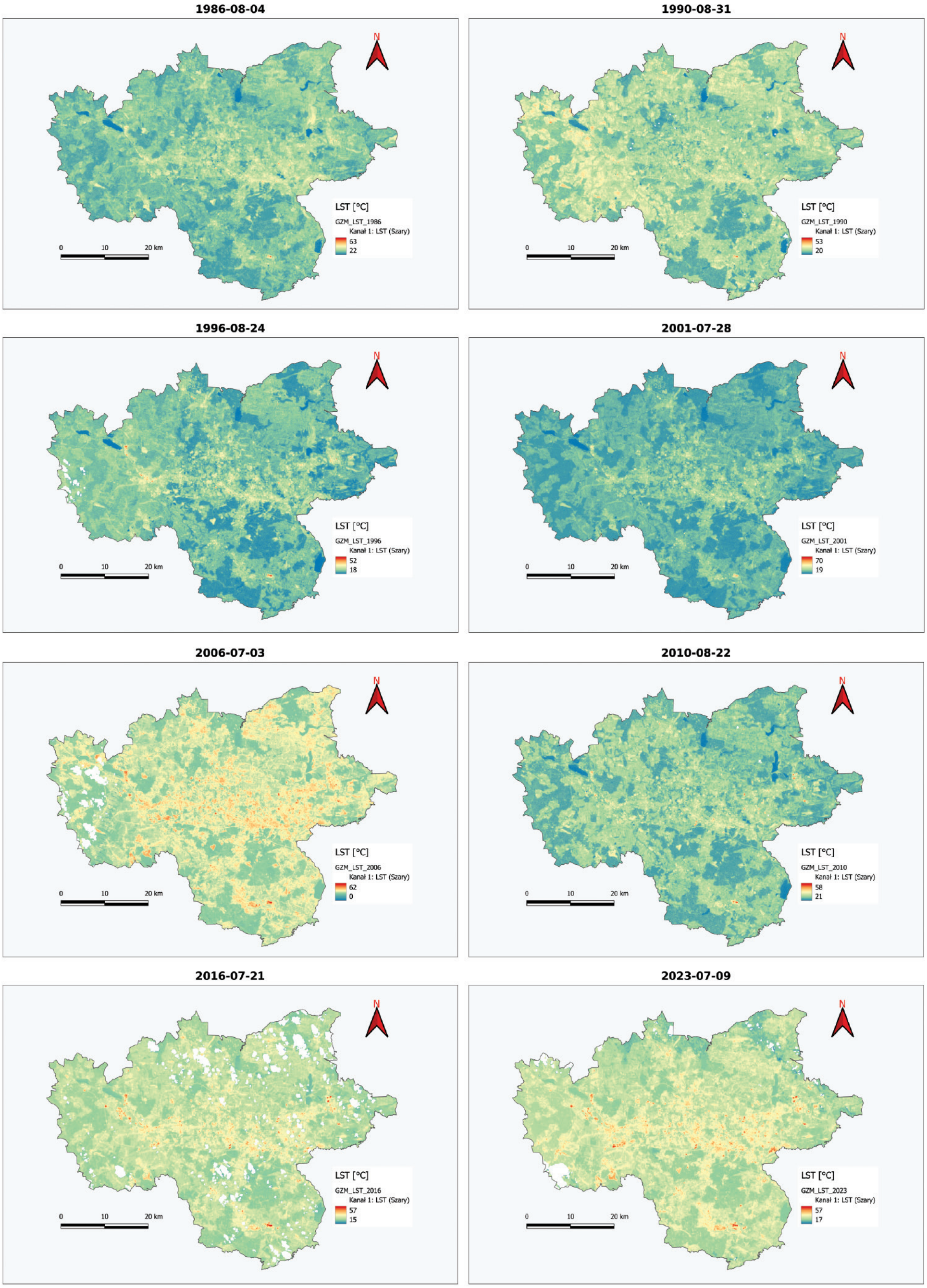

Source: Authors' own study

Fig. 6. Multi-temporal land surface temperature (LST) maps derived from Landsat data for the Upper Silesian–Dąbrowa Basin Metropolis (1986–2023)

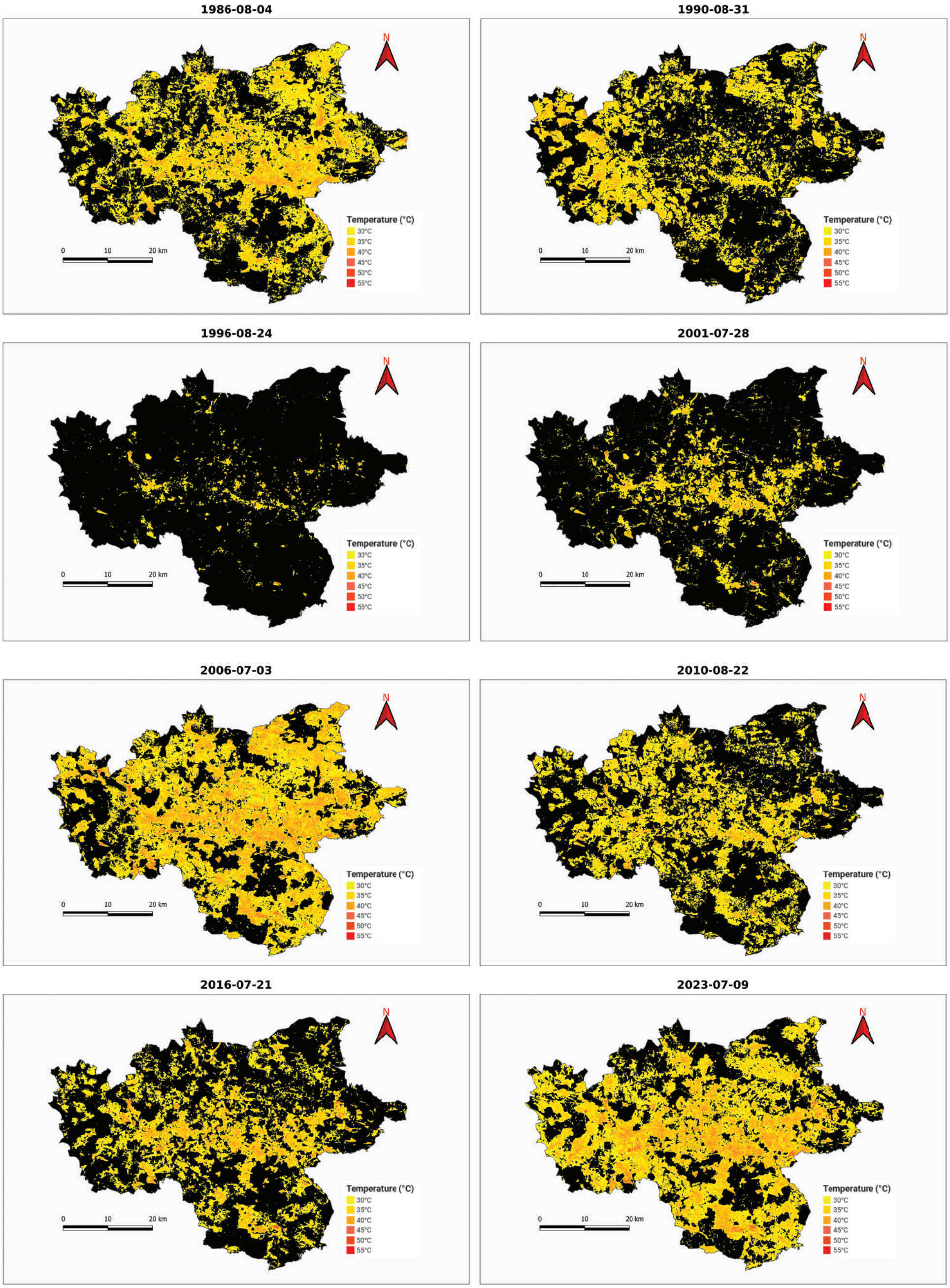

Source: Authors' own study

Fig. 7. Spatial distribution of high-LST hotspot areas, operationally defined as pixels with LST > 30°C, derived from multi-temporal Landsat data for the Upper Silesian–Dąbrowa Basin Metropolis (1986–2023)

The selected 2023 scene shows a greater extent of elevated LST than the selected 1986 scene in the three cities; however, the comparison remains sensitive to scene-specific meteorological conditions. In Katowice, higher temperatures are increasingly visible in the central and southern parts of the city, where dense urban fabric and transport infrastructure dominate. In Sosnowiec, the expansion of warm zones is particularly evident in areas associated with industrial and logistics functions. In Gliwice, clear thermal anomalies correspond to large industrial and warehouse complexes, including logistics parks such as Panattoni Park, as well as zones adjacent to major road infrastructure.

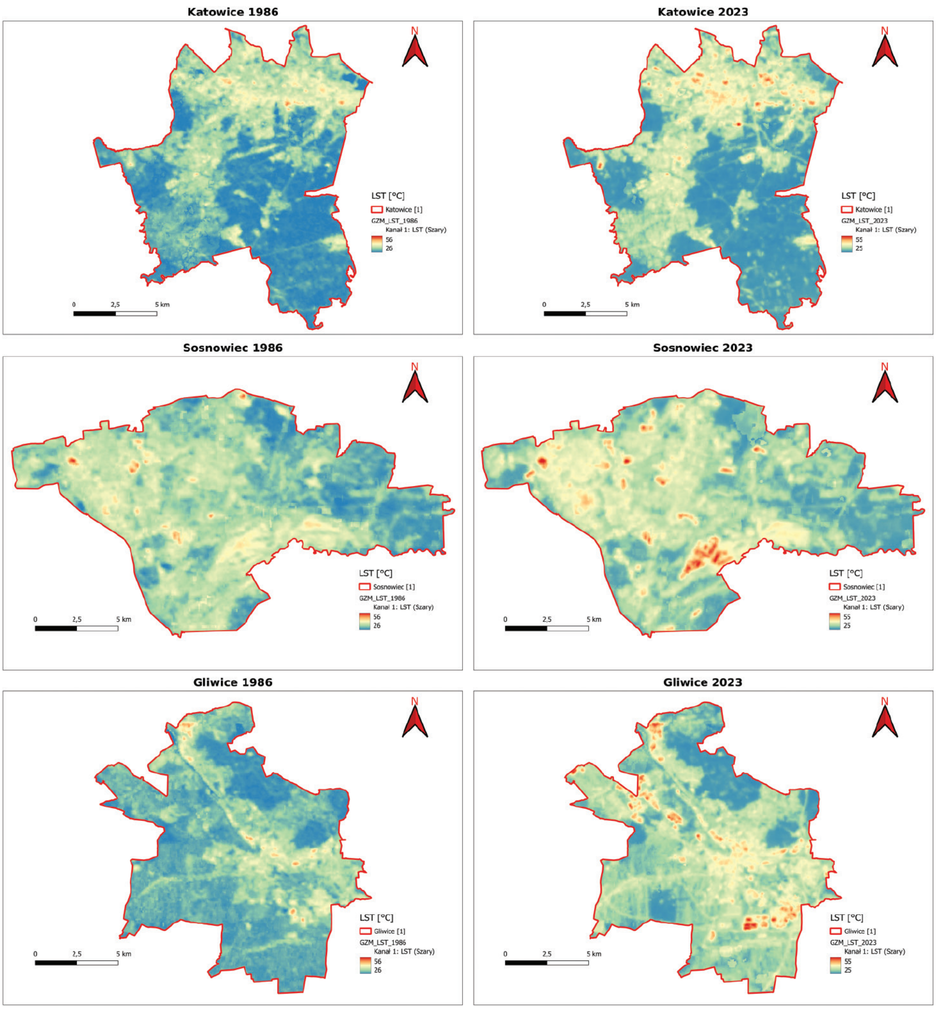

Source: Authors' own study

Fig. 8. Comparative spatial distribution of land surface temperature (LST) in 1986 and 2023 derived from Landsat data for the three selected major cities of the Upper Silesian–Dąbrowa Basin Metropolis: Katowice, Sosnowiec, and Gliwice

In all of the analysed cities, increased temperatures correspond to areas of intensified urban development and surface sealing, whereas forested and vegetated areas consistently act as local cooling zones.

The UAV imagery helps to explain what is contained within selected warm Landsat pixels. Although the 30 m Landsat grid does not resolve small features, the local UAV scenes show that these pixels often include roads, buildings, paved surfaces, and other small heat sources.

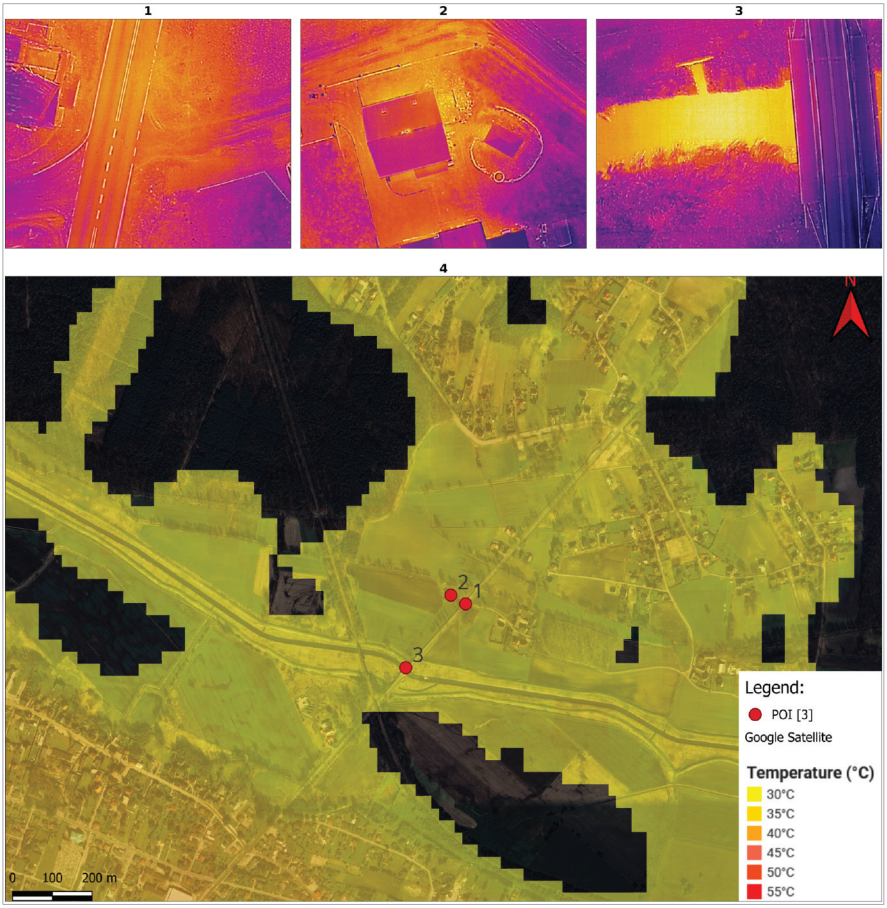

Source: Authors' own study

Fig. 9. Comparison of Landsat derived thermal pattern with high resolution UAV thermal imagery in the local study area within the Upper Silesian–Dąbrowa Basin Metropolis. Panels 1–3 show selected local features captured by UAV imagery: (1) road surface, (2) building and adjacent impervious surfaces, and (3) river corridor. Panel 4 shows their location within the Landsat based hotspot pattern. The comparison is intended to support local interpretation of spatial thermal contrasts rather than to validate absolute temperature values

For this reason, the UAV dataset should be treated as interpretive support rather than direct validation of absolute summer LST values. Its main contribution is to show the internal thermal heterogeneity of surfaces that appear as single pixels in Landsat imagery.

UAV data reveal substantially higher internal thermal variability within surfaces represented by single Landsat pixels and help identify point scale heat sources that remain unresolved in medium resolution imagery. These observations support the interpretation that elevated temperatures are closely associated with impervious materials and reduced vegetation cover, while adjacent vegetated areas tend to remain cooler.

Across all parts of the analysis, the same pattern is visible. Anthropogenic surfaces increased, agricultural land declined, and the thermal structure of the metropolis remained closely related to land cover. Conversion from agricultural land to anthropogenic surfaces was the main direction of change, while the UAV data helped explain local thermal contrasts within selected warm Landsat pixels.

4. Discussion

The pattern observed in the GZM does not suggest simple infill alone. The transition matrix shows that the dominant change was the conversion of agricultural land to anthropogenic surfaces, but the maps also reveal gradual reworking of older industrial land and mixed peri-urban zones. This combination fits the wider restructuring of a postindustrial metropolitan region and helps explain why some intermediate years show local reversals or mixed spectral signals rather than a perfectly monotonic trajectory [Renc and Łupikasza 2024, Rees et al. 2024].

The thermal pattern is best interpreted as a persistent spatial contrast rather than as a uniform year-to-year warming curve. Built-up, industrial, and transport areas remained the warmest parts of the landscape, whereas forest and water areas were cooler in most years. This interpretation is consistent with classic urban thermal remote sensing studies and with later Landsat based work showing that vegetation abundance and surface moisture tend to reduce heating, while impervious surfaces and development intensity strengthen it [Voogt and Oke 2003, Weng et al. 2004, Weng 2009, Xian and Crane 2006, Renc et al. 2022].

The relative cooling response of forest and water surfaces is not surprising, but the maps also show that not every vegetated patch plays the same role. In a fragmented metropolitan landscape, cooling depends not only on the presence of green or blue elements, but also on their size, continuity, and spatial context. This interpretation aligns with recent results from Krakow and to broader studies showing that the cooling effect of blue-green infrastructure varies with urban form, local climate zone, and landscape configuration [Głowienka and Micek 2025, Głowienka and Kucza 2025, Cureau et al. 2023, Li et al. 2022, Marquez-Torres et al. 2025, Zhang et al. 2025].

The UAV survey is valuable mainly because it reveals thermal contrasts that disappear within a 30 m satellite pixel. Roads, roofs, paved surfaces, and narrow strips of vegetation can generate marked local differences that are not visible in medium resolution imagery. Similar studies have shown that high resolution thermal data are especially useful at this local scale, where they help explain the broader satellite pattern [Heinemann et al. 2020, Coutts et al. 2016, Głowienka et al. 2025]. Because the UAV survey was carried out in winter and at a different time of day, it should still be treated as interpretive support rather than as direct validation of summer Landsat temperatures.

From a land management perspective, the present results point to a few practical priorities. The first is to limit additional sealing in districts that already form continuous warm belts. The second is to direct new development toward existing brownfield and redevelopment areas instead of further conversion of agricultural land. The third is to strengthen larger and more connected green and blue systems, especially where heat continuity is already visible along transport corridors and dense built-up zones. Remote sensing cannot replace ground based heat exposure studies, but it is very effective for locating persistent warm surfaces and identifying parts of the metropolitan landscape where mitigation is most urgent [Voogt and Oke 2003, Coutts et al. 2016, Manapragada et al. 2025, Renc and Łupikasza 2024].

Several limitations should be kept in mind. The analysis relies on medium resolution Landsat data, so mixed pixels are unavoidable in heterogeneous urban areas. The thermal comparison is based on individual cloud free reference scenes rather than on multi-date summer composites, which means that some inter-annual differences may still reflect day specific meteorological conditions. In addition, the classification was evaluated against manually interpreted test polygons rather than field data, and the UAV survey was acquired in winter rather than under the same summer conditions as the satellite scenes. These limitations do not negate the net differences observed between the selected endpoint maps, but they constrain causal and trend interpretation.

5. Summary and conclusions

The multi-temporal analysis shows a clear long-term shift in the land cover structure of the GZM. Anthropogenic surfaces increased overall, whereas agricultural land declined. At the same time, higher LST remained concentrated in built-up, industrial, and transport areas, while forest and water surfaces were consistently cooler.

The transition matrix indicates that the most important long term conversion was from agricultural land to anthropogenic surfaces. This pattern is consistent with urban expansion being a major driver of the mapped landscape restructuring. The Landsat archive revealed broad regional thermal patterns well, but the UAV survey also showed how much local variability remains hidden within single satellite pixels. For that reason, the UAV component is most useful as local interpretive support rather than as direct validation of Landsat derived summer temperatures.

In practical terms, the study identifies those parts of the GZM where land cover transformation and surface heating overlap most clearly. This is directly relevant to land management and climate adaptation, especially in areas where further surface sealing should be limited and where blue-green infrastructure, brownfield reuse, and the protection of larger vegetated areas should be prioritised.

References

Coutts A.M., Harris R.J., Phan T., Livesley S.J., Williams N.S.G., Tapper N.J. 2016. Thermal infrared remote sensing of urban heat: Hotspots, vegetation, and an assessment of techniques for use in urban planning. Remote Sensing of Environment, 186, 637–651. https://doi.org/10.1016/j.rse.2016.09.007

Cureau R.J., Pigliautile I., Pisello A.L. 2023. Seasonal and diurnal variability of a water body's effects on the urban microclimate in a coastal city in Italy. Urban Clim., 49, 101437. https://doi.org/10.1016/j.uclim.2023.101437

Duan S.B, Li Z.L., Zhao W., Wu P., Huang C., Han X.J., Gao M., Leng P., Shang G. 2021. Validation of Landsat land surface temperature product in the conterminous United States using in situ measurements from SURFRAD, ARM, and NDBC sites. International Journal of Digital Earth, 14(5), 640–660. https://doi.org/10.1080/17538947.2020.1862319

Głowienka E., Hejmanowska B., Michałowska K., Pękala A. 2017. Analysis of multitemporal changes in the environment using GIS and remote sensing in the aspect of construcion projects. Geomatics, Landmanagement and Landscape, 2, 61–69. https://doi.org/10.15576/GLL/2017.2.61

Głowienka E., Kucza M. 2025. Persistent Urban Park Cooling Effects in Krakow: A Satellite-Based Analysis of Land Surface Temperature Patterns (1990–2018). Remote Sensing, 17(21), 3608. https://doi.org/10.3390/rs17213608

Głowienka E., Malinverni E.S., Sanità M., Michałowska K., Kucza M. 2025. Harmonizing satellite thermal data with ground-based observations for climate long-term monitoring. International Archives of the Photogrammetry, Remote Sensing and Spatial Information Sciences XLVIII-M-7-2025, 127–132. https://doi.org/10.5194/isprs-archives-XLVIII-M-7-2025-127-2025

Głowienka E., Micek Z. 2025. Multitemporal assessment of Krakow's urban microclimate (2002–2023) using satellite-derived land surface temperature, NDVI, and NDBI. Geomatics, Landmanagement and Landscape, 3, 215–233. https://doi.org/10.15576/GLL/211223

Heinemann S., Siegmann B., Thonfeld F. et al. 2020. Land Surface Temperature Retrieval for Agricultural Areas Using a Novel UAV Platform Equipped with a Thermal Infrared and Multispectral Sensor. Remote Sensing, 12(7), 1075. https://doi.org/10.3390/rs12071075

Li X., Stringer L.C., Dallimer M. 2022. The role of blue green infrastructure in the urban thermal environment across seasons and local climate zones in East Africa. Sustainable Cities and Society, 80, 103798. https://doi.org/10.1016/j.scs.2022.103798

Malakar N.K., Hulley G.C., Hook S.J., Laraby K., Cook M., Schott J.R. 2018. An Operational Land Surface Temperature Product for Landsat Thermal Data: Methodology and Validation. IEEE Transactions on Geoscience and Remote Sensing, 56(10), 5717–5735. https://doi.org/10.1109/TGRS.2018.2824828

Manapragada N.V.S.K., Mandelmilch M., Roitberg E. et al. 2025. Remote sensing for environmentally responsive urban built environment: A review of tools, methods and gaps. Remote Sens. Appl. Soc. Environ., 38, 101529. https://doi.org/10.1016/j.rsase.2025.101529

Marquez-Torres A., Kumar S., Aznarez C., Jenerette G.D. 2025. Assessing the cooling potential of green and blue infrastructure from twelve US cities with contrasting climate conditions. Urban For Urban Green, 104, 128660. https://doi.org/10.1016/j.ufug.2024.128660

Rees G., Hebryn-Baidy L., Belenok V. 2024. Temporal Variations in Land Surface Temperature within an Urban Ecosystem: A Comprehensive Assessment of Land Use and Land Cover Change in Kharkiv, Ukraine. Remote Sens., 16, 1637. https://doi.org/10.3390/rs16091637

Renc A., Łupikasza E. 2024. Changes in the surface urban heat island between 1986 and 2021 in the polycentric Górnośląsko-Zagłębiowska Metropolis, southern Poland. Build Environ., 247, 110997. https://doi.org/10.1016/j.buildenv.2023.110997

Renc A., Łupikasza E., Błaszczyk M. 2022. Spatial structure of the surface heat and cold islands in summer based on Landsat 8 imagery in southern Poland. Ecol. Indic., 142, 109181. https://doi.org/10.1016/j.ecolind.2022.109181

Rouse J.W. Jr., Haas R.H., Deering D.W., Schell J.A. 1973. Monitoring the vernal advancement and retrogradation (green wave effect) of natural vegetation. Final Report, Remote Sensing Center, Texas A&M University, College Station, Texas. NASA/GSFC, Greenbelt, MD, USA.

Roy D.P., Wulder M.A., Loveland T.R. et al. 2014. Landsat-8: Science and product vision for terrestrial global change research. Remote Sens. Environ., 145, 154–172. https://doi.org/10.1016/j.rse.2014.02.001

Voogt J.A., Oke T.R. 2003. Thermal remote sensing of urban climates. Remote Sensing of Environment, 86(3), 370–384. https://doi.org/10.1016/S0034-4257(03)00079-8

Weng Q. 2009. Thermal infrared remote sensing for urban climate and environmental studies: Methods, applications, and trends. ISPRS Journal of Photogrammetry and Remote Sensing, 64(4), 335–344. https://doi.org/10.1016/j.isprsjprs.2009.03.007

Weng Q., Lu D., Schubring J. 2004. Estimation of land surface temperature–vegetation abundance relationship for urban heat island studies. Remote Sensing of Environment, 89(4), 467–483. https://doi.org/10.1016/j.rse.2003.11.005

Xian G., Crane M. 2006. An analysis of urban thermal characteristics and associated land cover in Tampa Bay and Las Vegas using Landsat satellite data. Remote Sensing of Environment, 104(2), 147–156. https://doi.org/10.1016/j.rse.2005.09.023

Zha Y., Gao J., Ni S. 2003. Use of normalized difference built-up index in automatically mapping urban areas from TM imagery. Int. J. Remote Sens., 24, 583–594. https://doi.org/10.1080/01431160304987

Zhang L., Wang S., Zhai W. et al. 2025. How does Blue-Green Infrastructure affect the urban thermal environment across various functional zones? Urban For Urban Green, 105, 128698. https://doi.org/10.1016/j.ufug.2025.128698

Zhao J., Yu L., Zhao L. et al. 2025. Significant contribution of urban morphological diversity to urban surface thermal heterogeneity. Urban Clim., 61, 102383. https://doi.org/10.1016/j.uclim.2025.102383

Zuzańska-Żyśko E., Sitek S. 2018. Górnośląsko-Zagłębiowska Metropolia w kontekście wyzwań społeczno-gospodarczych. Górnośląskie Studia Socjologiczne, Ser. Nowa, 9, 68–80. https://doi.org/10.31261/GSS_SN.2018.09.02.04